

Cooling rate dependence of structural order in $\text{Ni}_{62}\text{Nb}_{38}$ metallic glass

Tongqi Wen, Yang Sun, Beilin Ye, Ling Tang, Zejin Yang, Kai-Ming Ho, Cai-Zhuang Wang, and Nan Wang

Citation: *Journal of Applied Physics* **123**, 045108 (2018); doi: 10.1063/1.5019681

View online: <https://doi.org/10.1063/1.5019681>

View Table of Contents: <http://aip.scitation.org/toc/jap/123/4>

Published by the *American Institute of Physics*

Articles you may be interested in

[Local environments of atomic clusters and the effect on dynamics in CuZr metallic glass-forming liquids](#)

Journal of Applied Physics **122**, 225103 (2017); 10.1063/1.5004262

[Absolute determination of optical constants of three transition metals using reflection electron energy loss spectroscopy](#)

Journal of Applied Physics **123**, 043306 (2018); 10.1063/1.5012013

[Effects of Al addition on atomic structure of Cu-Zr metallic glass](#)

Journal of Applied Physics **123**, 055101 (2018); 10.1063/1.5008841

[Atomic structure and dynamics properties of \$\text{Cu}_{50}\text{Zr}_{50}\$ films](#)

Journal of Applied Physics **123**, 025307 (2018); 10.1063/1.5011122

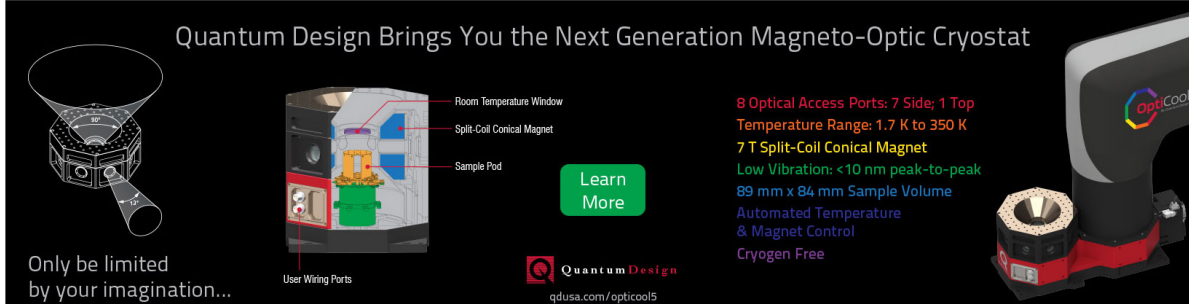
[Structural modification through pressurized sub- \$T_g\$ annealing of metallic glasses](#)

Journal of Applied Physics **122**, 215106 (2017); 10.1063/1.5004058

[Brittle to ductile transition of metallic glasses induced by embedding spherical nanovoids](#)

Journal of Applied Physics **122**, 215108 (2017); 10.1063/1.4997281

Quantum Design Brings You the Next Generation Magneto-Optic Cryostat



Only be limited by your imagination...

Room Temperature Window
Split-Coil Conical Magnet
Sample Pod
User Wiring Ports

[Learn More](#)

Quantum Design
qdusa.com/opticool5

8 Optical Access Ports: 7 Side; 1 Top
Temperature Range: 1.7 K to 350 K
7 T Split-Coil Conical Magnet
Low Vibration: <10 nm peak-to-peak
89 mm x 84 mm Sample Volume
Automated Temperature & Magnet Control
Cryogen Free

OptiCool

Cooling rate dependence of structural order in $\text{Ni}_{62}\text{Nb}_{38}$ metallic glass

Tongqi Wen,^{1,2} Yang Sun,² Beilin Ye,³ Ling Tang,^{2,4} Zejin Yang,^{2,4} Kai-Ming Ho,^{2,5} Cai-Zhuang Wang,^{2,5,a)} and Nan Wang^{1,a)}

¹MOE Key Laboratory of Materials Physics and Chemistry under Extraordinary Conditions, School of Natural and Applied Sciences, Northwestern Polytechnical University, Xi'an 710072, China

²Ames Laboratory-USDOE, Iowa State University, Ames, Iowa 50011, USA

³School of Materials Science and Engineering, South China University of Technology, Guangzhou 510640, China

⁴Department of Applied Physics, College of Science, Zhejiang University of Technology, Hangzhou 310023, China

⁵Department of Physics and Astronomy, Iowa State University, Ames, Iowa 50011, USA

(Received 15 December 2017; accepted 14 January 2018; published online 31 January 2018)

Molecular dynamics (MD) simulations are performed to study the structure of $\text{Ni}_{62}\text{Nb}_{38}$ bulk metallic glass at the atomistic level. Structural analysis based on the cluster alignment method is carried out and a new Ni-centered distorted-icosahedra (DISICO) motif is excavated. We show that the short-range order and medium-range order in the glass are enhanced with lower cooling rate. Almost 50% of the clusters around the Ni atoms in the well-annealed $\text{Ni}_{62}\text{Nb}_{38}$ glass sample from our MD simulations can be classified as DISICO. It is revealed that the structural distortion with respect to the perfect icosahedra is driven by chemical ordering in the distorted region of the DISICO motif. The relationship between the structure, energy, and dynamics in this glass-forming alloy during the cooling and annealing processes is also established. *Published by AIP Publishing.*

<https://doi.org/10.1063/1.5019681>

I. INTRODUCTION

Since the first discovery of the metallic glass (MG),¹ extensive studies have shown that many MGs possess special short-range order (SRO) structures^{2–5} and unusual properties.^{6–9} Among the unsolved problems, the relationship between the atomic-level structure and the properties is a fundamental one and has aroused intensive interest in the past few years.^{10,11} In many cases, the number of chemical elements in MGs is more than three,¹² making the study on the structural order at the atomistic level more difficult. Fortunately, binary MGs have recently been found in systems like Cu-Zr,^{13–16} Pd-Si,¹⁷ Ni-Nb,^{18–20} Al-Sm,²¹ etc., and many studies on the structure-property relationship were carried out in these binary systems.^{22–26}

The Ni-Nb binary alloy at the eutectic composition, i.e., $\text{Ni}_{59.5}\text{Nb}_{40.5}$, was shown to be a good glass former about 4 decades ago.¹⁸ Glass formation at other compositions in the Ni-Nb binary system was also reported in later studies. For example, Zhu *et al.*¹⁹ reported that 1.5 mm diameter fully amorphous rods of binary $\text{Ni}_{61.5}\text{Nb}_{38.5}$ can be fabricated by copper mold injection casting methods. Xia *et al.*²⁰ studied the glass-forming ability (GFA) in $\text{Ni}_x\text{Nb}_{100-x}$ ($x = 59.5, 60.5, 61, 61.5, 62, \text{ and } 62.5$) binary alloys and found that the best glass former is an off-eutectic $\text{Ni}_{62}\text{Nb}_{38}$ alloy which can be cast into fully glassy rods up to 2 mm in diameter. However, the studies on the structure-property relationship in the best Ni-Nb glass former, i.e., $\text{Ni}_{62}\text{Nb}_{38}$, are still very few. Tian *et al.*²⁷ performed *ab initio* molecular dynamics (MD) simulation on $\text{Ni}_{62.5}\text{Nb}_{37.5}$ and found that the

icosahedra (ICO) motif exists in the liquid and becomes dominant in the amorphous state. This study sheds light on the atomistic structure of the amorphous state, but the glassy sample produced is under the cooling rate of more than 10^{13} K/s and limited by the atomic numbers in the model (only 200 atoms). Very recently, Zhang *et al.*²⁸ developed a semi-empirical potential of the Finnis-Sinclair (FS) type²⁹ and performed MD simulations to show that a network in combination of ICO clusters centered on Ni atoms with Z14, Z15, and Z16²⁸ clusters centered on Nb atoms would be responsible for the glass formation in this system. Moreover, Xu *et al.*³⁰ applied this new-released potential and found that the calculated pair correlation functions and structure factors match well with the experimental data in the compositions $\text{Ni}_x\text{Nb}_{1-x}$ ($x = 50\text{--}70$ at. %). They also reveal that the dynamics is insensitive to the compositions in Ni-Nb alloys, which are quite different from Cu-Zr alloys. However, the main difference between simulation and experiment is that the cooling rate employed in the former (normally faster than 10^9 K/s) is much larger than that in the latter ($\sim 10^3\text{--}10^6$ K/s). Consequently, further studies to investigate the cooling rate dependence of the structural order in this system are desirable.

Recently, a sub- T_g annealing method³¹ which anneals the sample just below and close to the glass transition temperature (T_g) is applied to achieve the effective lower cooling rate and has been shown to be effective in Cu-Zr³² and Al-Sm³³ systems. In the present study, we employ the sub- T_g annealing method on $\text{Ni}_{62}\text{Nb}_{38}$ MG to investigate the evolution of structural order. The MG sample of $\text{Ni}_{62}\text{Nb}_{38}$ has been achieved with an effective cooling rate of 1.58×10^8 K/s and the structure factor $S(q)$ of the sub- T_g annealed

^{a)}Authors to whom correspondence should be addressed: wangcz@ameslab.gov and nan.wang@nwpu.edu.cn

sample is closer to that of measured by experiment. In order to characterize the structure motif, cluster alignment^{34,35} and pair-wise alignment plus clique analysis methods²⁴ are applied on the glassy samples generated from the MD simulations. A new distorted-icosahedra (DISICO) motif is found to be dominant in the glass samples. Comparing the samples with different cooling processes, the evolution of short-range order (SRO) and medium-range order (MRO) is investigated. Finally, the connection between the structure, energy and dynamics is studied through the cooling and annealing processes. In the cooling process, the “crossover” phenomenon^{36–38} which denotes the deviation of diffusion coefficient from the Arrhenius behavior as the temperature is lowered is observed which is found to be accompanied by the boom of SRO.

II. SIMULATION DETAILS AND ANALYSIS METHODS

Molecular dynamics simulation with an *NPT* ensemble at zero pressure is carried out on a $\text{Ni}_{62}\text{Nb}_{38}$ system by using the LAMMPS package³⁹ and the periodic boundary conditions are applied through the whole process. The time step of the simulation is 2.5 fs. The liquid sample with 3100 Ni atoms and 1900 Nb atoms is initially equilibrated at 2000 K for 2.5 ns and then cooled down continuously to 300 K at the rate of 10^9 , 10^{10} , 10^{11} , 10^{12} , and 10^{13} K/s, respectively. The samples at the cooling rate from 10^{10} to 10^{13} K/s are repeated five times and the simulation at 10^9 K/s is repeated three times by changing the initial velocity. In Fig. 1, the energy change in the cooling process at 10^{10} K/s is plotted. T_g is determined to be around 1000 K and the sub- T_g annealing method is then applied on the 10^{10} K/s quenched sample at 950 K for 2.0 μs , followed by a continuous quenching to 300 K at 10^{10} K/s. MD trajectories over 500 ps are used to calculate the averaged atomic positions at 300 K to remove the thermal vibration effects. At other temperatures, the inherent structures which are obtained by freezing structures rapidly are used for structural analysis.

Cluster alignment^{34,35} and pair-wise alignment/clique methods²⁴ are carried out on the samples with different cooling processes to excavate and characterize the atomistic

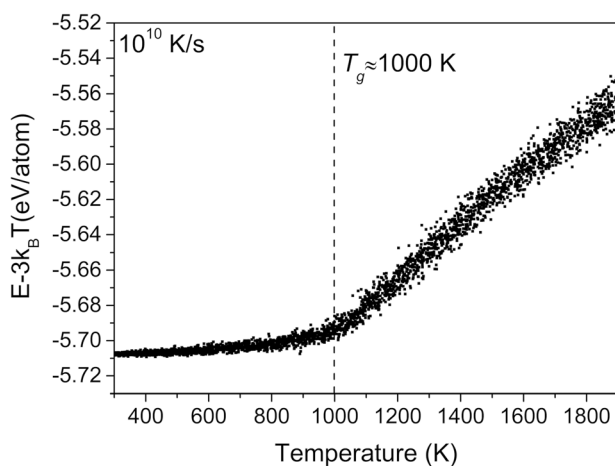


FIG. 1. Change in energy during cooling the $\text{Ni}_{62}\text{Nb}_{38}$ liquid from 2000 K to 300 K at the cooling rate of 10^{10} K/s.

SRO in the samples. For the cluster alignment method, an alignment score is calculated to define how much the aligned cluster deviates from the motif in a given template^{24,33}

$$f = \min_{0.80 \leq \alpha \leq 1.2} \left(\frac{1}{N} \sum_{i=1}^N \frac{(\vec{r}_{ic} - \alpha \vec{r}_{it})^2}{(\alpha \vec{r}_{it})^2} \right)^{1/2}, \quad (1)$$

where N is the number of neighbor atoms in the template, r_{ic} and r_{it} are the atomic positions in the aligned cluster and template, respectively, and α is a coefficient to adapt the template's bond length. In order to achieve an optimal alignment, the range of α is chosen between 0.8 and 1.2 which helps the aligned cluster match with the template. The smaller score indicates the higher similarity between the aligned cluster and the motif in the template.

The pair-wise alignment²⁴ is based on the cluster alignment method^{34,35} and the difference is that the clusters centered on the same type of atom are aligned with each other instead of using templates. It computes a similarity matrix with $N(N-1)/2$ alignment scores for N clusters. Then, the maximal clique analysis²⁴ is applied to explore the dominant structural motif among the aligned clusters.

III. RESULTS AND DISCUSSION

A. Effective cooling rate by sub- T_g annealing

First, the effectiveness of the sub- T_g annealing is studied from the aspect of the potential energy as plotted in Fig. 2. A linear dependence of potential energy on the logarithm of the cooling rate is observed for the continuously cooled samples, which is also seen in Cu-Zr,^{31,32} Al-Sm,³³ and Ni-Zr⁴⁰ systems. The potential energy decreases by 5 to 6 meV/atom when the cooling rate is lowered by an order of magnitude. Assuming that this linear relationship persists for even lower cooling rates, extrapolation of the linear dependence yields effective cooling rates of 1.58×10^8 K/s after annealing at 950 K for 2.0 μs . The total simulation time for the continuous quenching at this cooling rate would be 10.76 μs . Therefore,

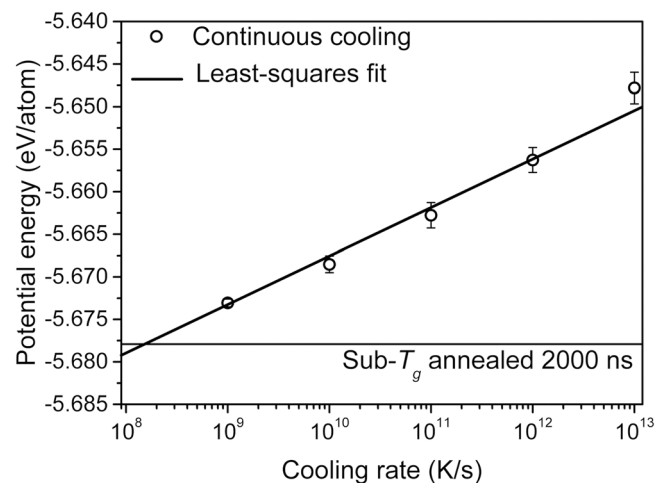


FIG. 2. Potential energy at 300 K as the function of cooling rate. The thick line indicates the least-squares fitting to a logarithm dependence of all continuously quenched samples. The effective cooling rate equals to 1.58×10^8 K/s by sub- T_g annealing at 950 K for 2 μs .

the sub- T_g annealing speeds up the simulation by a factor of 5 for this system.

B. Partial pair correlation functions and structure factor

The sub- T_g annealed sample is accomplished with a lower effective cooling rate and thus closer to the experiment. Now we investigate the evolution of structural order in glassy samples with different cooling processes. The partial correlation functions $g(r)$ for the samples with different cooling rates are displayed in Figs. 3(a)–3(c) and we can see that the overall shapes of the $g(r)$ s do not change much with different cooling rates, but the relative heights and positions of the peaks in the $g(r)$ s are dependent on the cooling rate. For $g_{\text{Ni-Ni}}(r)$ and $g_{\text{Ni-Nb}}(r)$, both the first and the second peaks are enhanced with decreasing cooling rate indicating that SRO and MRO are more developed around the Ni atoms in the sample. The development of SRO and MRO upon slower cooling can be seen more clearly by using the cluster

alignment analysis as will be discussed later in this paper. For $g_{\text{Nb-Nb}}(r)$, the height of the first peak slightly decreases, but the second peak is obviously strengthened with the lower cooling rate and in the sub- T_g annealing, which can be explained as “solute-solute avoidance.”⁴¹ The positions of the first peak in $g(r)$ are around 2.49 Å, 2.61 Å, and 3.03 Å for $g_{\text{Ni-Ni}}(r)$, $g_{\text{Ni-Nb}}(r)$, and $g_{\text{Nb-Nb}}(r)$, respectively. The Ni-Nb distance (2.61 Å) is shorter than the average value (2.76 Å) of the Ni-Ni and Nb-Nb bond lengths, suggesting the enhanced Ni-Nb bonding attributed to the charge transfer between Ni and Nb.²⁷ The evolution of the structure factor $S(q)$ with the cooling rate is plotted in Fig. 3(d) and the equations for calculation are listed in Ref. 33. When comparing with the experimental data from Ref. 28, we observe that $S(q)$ of the sub- T_g annealed sample with the enhanced first peak is closer to the X-ray data. The simulation results fit the experimental data pretty well which validates the potential employed in this study. From the results of potential energy, pair correlation functions, and the comparison of the structure factor with experiment, the sub- T_g annealing process is

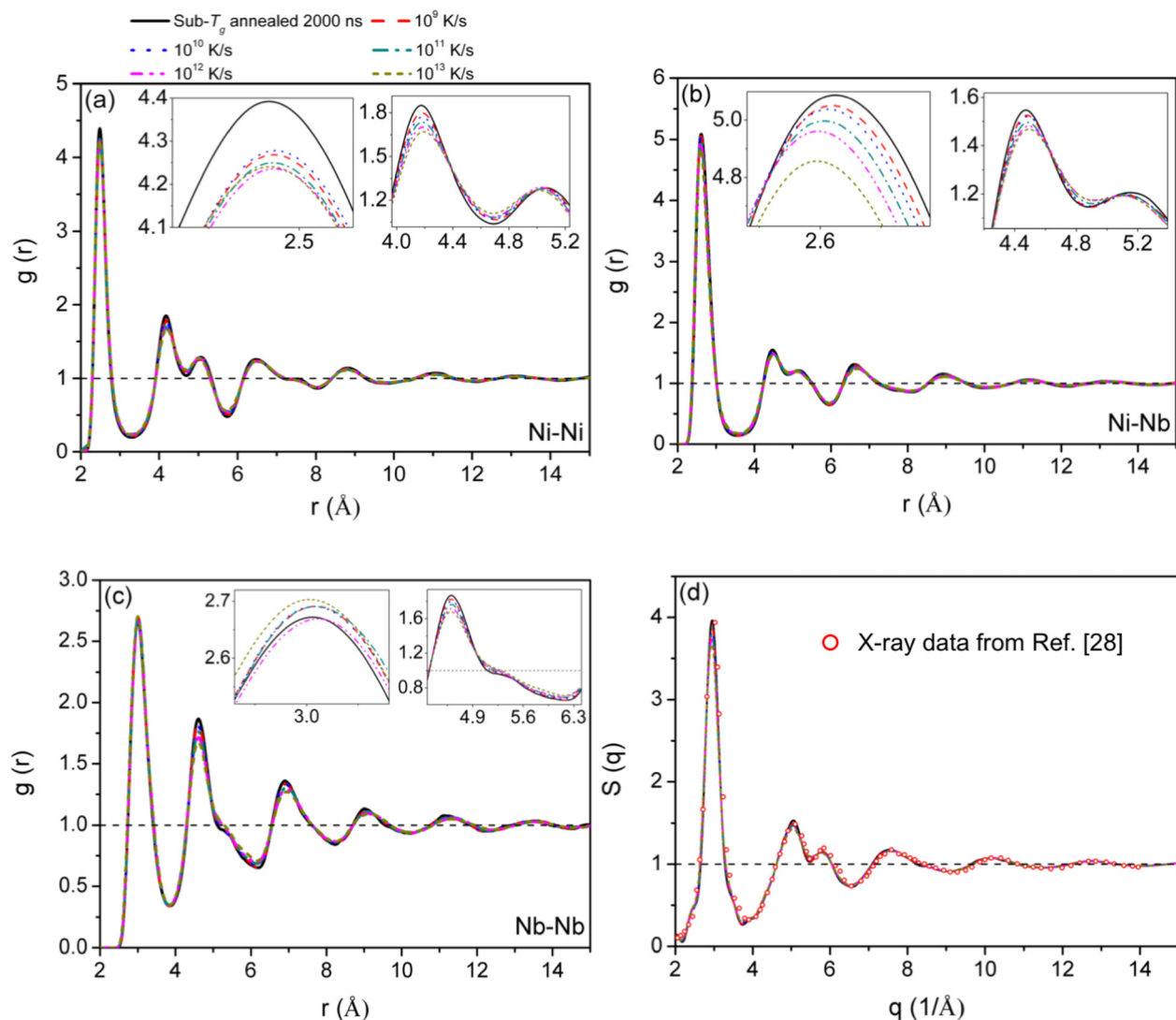


FIG. 3. (a)–(c) Partial pair correlation functions of Ni-Ni, Ni-Nb, and Nb-Nb at 300 K for the $\text{Ni}_{62}\text{Nb}_{38}$ glassy samples with different cooling processes. The insets zoom in the first and second peaks. (d) The total structure factors of the glassy samples at 300 K with different cooling rates and from the X-ray experiment.

effective and a more stable and relaxed glassy sample is produced.

C. Structural and chemical order

From the pair correlation functions, the coordination numbers determined for Ni and Nb are around 12.2 and 15.4, respectively, by using the first minimum of $g(r)$ as the cutoff. In order to excavate and characterize the SRO in the glassy samples, we first apply pair-wise alignment and clique analysis²⁴ on the sub- T_g annealed glassy sample to identify the dominant local order motif for this system. A new motif centered on Ni obtained from our analysis is plotted in Fig. 4(a). Compared with the perfect ICO shown in Fig. 4(b), the cluster shown in Fig. 4(a) exhibits considerable distortions from the perfect ICO, particularly at the right-bottom part of the cluster (the sites colored in brown and orange and included in the dashed circle). As a result, two pentagons in the perfect ICO shrink to two approximate quadrangles in the distorted ICO cluster which intersect at the brown sites. In the following paragraph, we name this new distorted ICO motif “DISICO” for short.

Using the newly identified DISICO along with other commonly used²⁸ BCC, FCC, HCP, and ICO for Ni-centered templates, and BCC, FCC, HCP, ICO, Z14, Z15, and Z16 (the structure of Z14, Z15, and Z16 can be found in Ref. 10) for Nb centered templates, cluster-template one-on-one alignment analysis is performed on all Ni- and Nb-centered clusters extracted from the glassy sample generated by MD

simulations at different cooling rates (including the one from sub- T_g annealing).

The distribution of the alignment scores for Ni- and Nb-centered clusters in the sub- T_g annealed glassy samples at 300 K is shown in Figs. 4(c) and 4(d), respectively. When the alignment score cutoff of 0.15 is used to assign both the Ni- and Nb-centered clusters to different motifs, DISICO and ICO are found to be the dominant SRO covering 49.10% and 10.74% of the total Ni-centered clusters, respectively. The high fraction of distorted and perfect ICO implies good GFA of this system. As for the Nb-centered motifs, Z14, Z15, and Z16 are found to be the abundant ones with the fraction of 8.11%, 18.16%, and 5.16% of the total Nb-centered clusters, respectively. The dominant motifs in Ni- and Nb-centered clusters agree with their own coordination numbers calculated from the pair correlation functions.

In almost all the cluster alignment analyses in previous studies, only geometry is considered without distinguishing the chemical identity of atoms in each position. By including the chemical identity of the atoms around the positions of the template after alignment,³⁴ we can investigate not only the geometrical structure order but also the chemical order of the clusters in the glass samples. The distribution of the Ni and Nb atoms around each atomic position of the DISICO and ICO templates is shown in Figs. 5(a) and 5(c), respectively. The small red dots denote Ni atoms and the blue ones represent Nb atoms. The color scheme for the template is the same as that used in Figs. 4(a) and 4(b). Each position is labeled and the chemical order at each site is

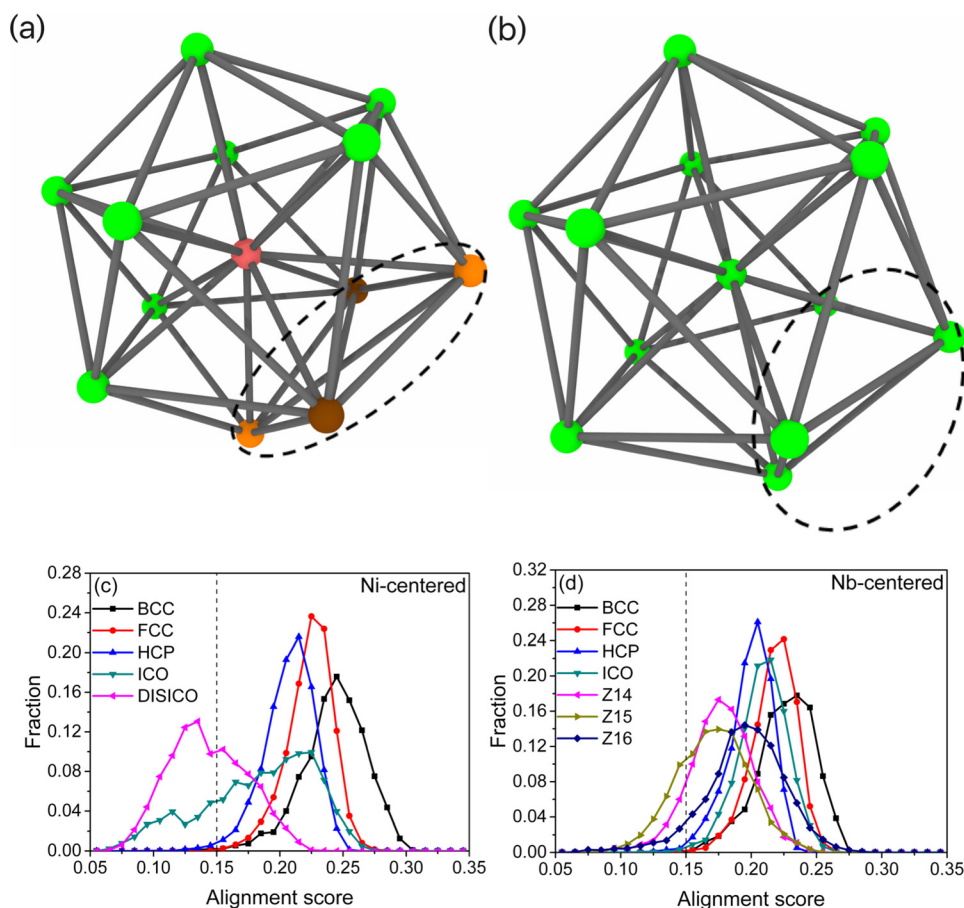


FIG. 4. (a) DISICO motif. The orange and brown balls represent the atoms with much deviation from the perfect ICO. (b) Perfect ICO cluster. In (a) and (b), the dashed circles are used to indicate the region where DISICO is different from ICO. (c) and (d) are the distribution of alignment scores of Ni- and Nb-centered clusters in the sub- T_g annealed glassy sample at 300 K, respectively. The cutoff 0.15 is used to classify both the Ni- and Nb-centered motifs.

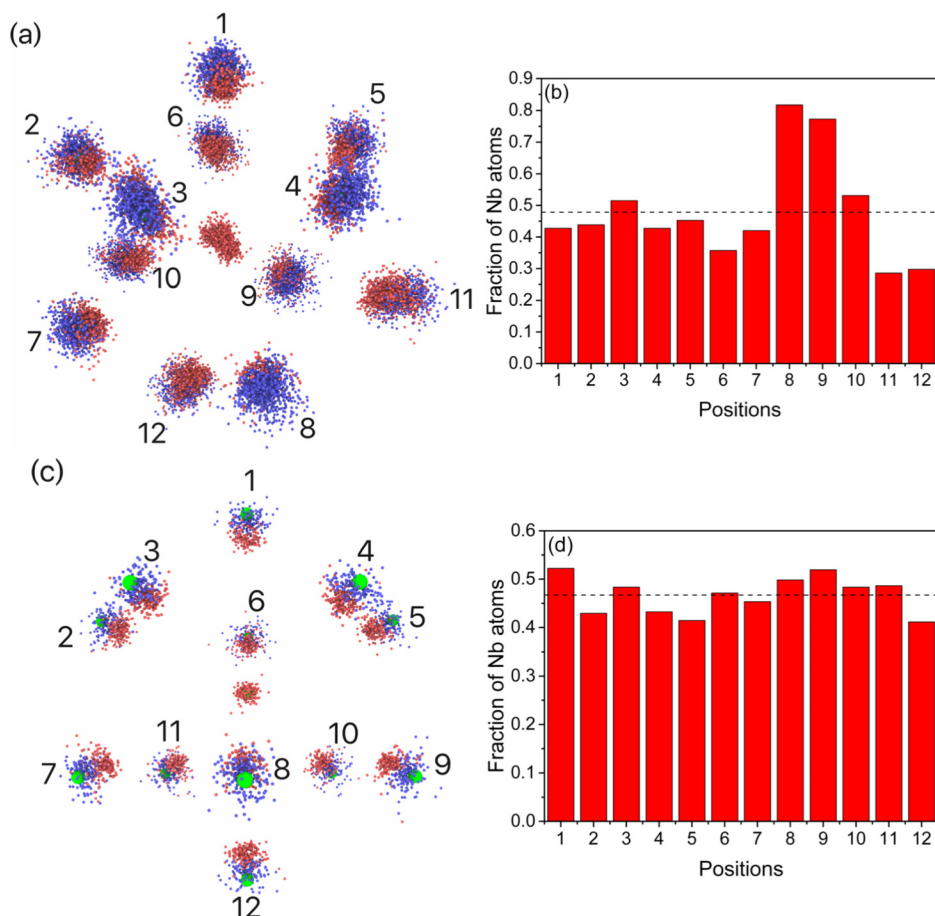


FIG. 5. Chemical order in (a) and (b): DISICO, (c) and (d): ICO, respectively. The usage of the colors of the template is the same as that in Figs. 4(a) and 4(b). The small red balls represent Ni and the blue ones are Nb. The dashed line denotes the total fraction of Nb atoms in all labeled positions.

characterized by the fraction of Nb atoms at this site. The corresponding fraction of Nb atoms in each position for DISICO and ICO motifs is displayed in Figs. 5(b) and 5(d), respectively. The total fractions of Nb in all positions around the center Ni atom are about 0.47 for both motifs indicating the similarity between them. The fraction of Nb in ICO and DISICO is higher than the stoichiometry 38% in the composition which can be explained as follows. From Figs. 3(a)–3(c), we can find that the height of the first peak in $g(r)$ between Ni-Nb is the highest among the three indicating that Ni atoms are more prone to be surrounded by a different type of atom, Nb. Using the first minimum of each partial $g(r)$ as the cutoff, we can calculate the partial coordination number for each type of atom within the first shell. For the sub- T_g annealed sample, Ni is surrounded by 6.24 Ni and 5.95 Nb atoms and Nb is surrounded by 9.70 Ni and 5.73 Nb atoms on average. The fraction of Nb atoms within the first shell of Ni is 0.49 (not including the center Ni) which is higher than 0.38. When we look into the chemical order for each position, the difference between DISICO and ICO SRO can be seen. For the DISICO, on the one hand, positions 8 and 9 (colored in brown) are occupied with much more Nb atoms than the average value and these two positions form the intersection of the two quadrangle faces. On the other hand, Nb atoms are poor in positions 11 and 12 (colored in orange) and these two positions are among the 4 sites mostly distorted from the perfect ICO. As for the ICO motif, the fraction of Nb atoms in all positions is within the range of 0.47 ± 0.05 , indicating the equivalence of all positions in the

motif. From this perspective, the differences between DISICO and ICO motifs are demonstrated from the view point of both the geometry and the chemical order and they are connected firmly with each other. Although the alignment and pair-wise alignment methods have also been used in Refs. 24 and 33, the analysis of chemical order in the present paper is new and gives much more useful insight into SRO in the metallic glass. Our analysis results demonstrate that the chemical order can affect the geometrical structure order and *vice versa*.

D. Evolution of the structural order

Figure 6(a) shows the fractions of major Ni- and Nb-centered clusters at 300 K with different effective cooling rates. We can see that the fractions of all the major SRO clusters increase as the effective cooling rate decreases, indicating that a more stable and relaxed glassy sample was generated from MD simulation with a lower cooling rate. For Ni-centered ICO and Nb-centered Z14, Z15, and Z16 motifs, their fraction in the sub- T_g annealed glassy sample increases by about 60% in comparison with those in the sample generated at a cooling rate of 10^{13} K/s. As for the Ni-centered DISICO motif, the fraction is already very large in the fastest-quenched sample and decreasing the cooling rate continues to enhance such a SRO. In Fig. 6(b), the fractions of the dominant Ni- and Nb-centered clusters at different temperatures under a cooling rate of 10^{10} K/s are displayed. It is observed that at temperatures higher than 1400 K, the

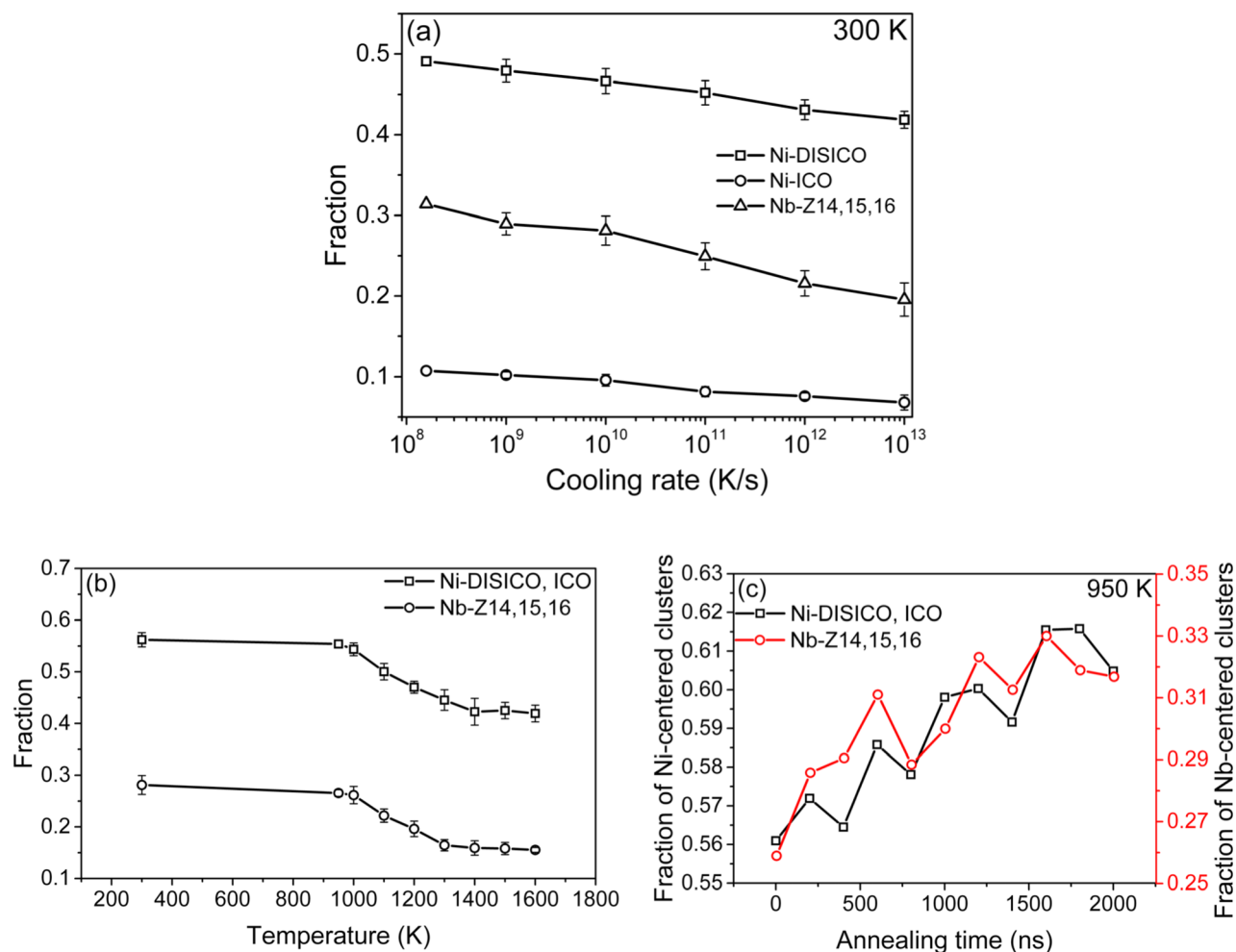


FIG. 6. (a) The change of the fractions of Ni- and Nb-centered motifs at 300 K with effective cooling rates; (b) Fractions of the Ni- and Nb-centered SRO at different temperatures with 10^{10} K/s cooling rate; (c) Fraction of the Ni- and Nb-centered SRO in the sub- T_g annealing process at 950 K.

fractions of the Ni- and Nb-centered SRO remain almost constant. When the temperature is lower than 1300 K, the SRO develops significantly implying that the system jumps out the basins belonging to the high temperature and starts to visit the basins with lower potential energy on the energy landscape. In this study, we also carry out a 2000 ns sub- T_g annealing just below T_g and it is of high interest to investigate the evolution of the SRO during this process. Figure 6(c) plots the fraction of the dominant motifs centered on Ni and Nb by every 200 ns during the annealing process. Both the Ni- and Nb- centered motifs are observed to increase in the annealing process and a higher fraction of SRO indicates a more stable amorphous sample which explains the lower potential energy after sub- T_g annealing as shown in Fig. 2.

E. Medium-range order

After studying the evolution of the SRO, we extend the analysis to the MRO to see how the SRO clusters in the glass samples are connected. Here, we focus on the MRO among the dominant Ni-centered motifs. The radial distribution function of the center atoms of the DISICO and ICO clusters, $G_c(r) = 4\pi r^2 \rho_c g_c(r)$, is introduced to show the correlation among the clusters where $g_c(r)$ is the pair correlation

function calculated only for the center Ni atom in DISICO or ICO and ρ_c is their corresponding number density in the sample. Figures 7(a) and 7(b) show the $G_c(r)$ from the center atoms of the DISICO and ICO clusters at different effective cooling rates, respectively. It is clear that the first peak of the $G_c(r)$ for the ICO centers is much higher than the second and third peaks suggesting the tendency for ICO to be interpenetrated.³² For DISICO, however, the intensity of the first peak in their $G_c(r)$ is not as high as that of the second and third peaks indicating much less interpenetrated DISICO clusters as compared to the perfect ICO. All peaks in the $G_c(r)$ of ICO are enhanced with decreasing cooling rate. As for the DISICO, the first peak is much less sensitive to the cooling rate, while the second and third peaks become more intense with lowering the cooling rate. In this case, the distortions in DISICO make this motif less efficient for interpenetrating packing. Figures 7(c) and 7(d) show some typical networks of the DISICO clusters and the different types of connections. There are 4 types of connections between DISICO. In Fig. 7(c), the atoms in red show the connection of interpenetrating between DISICO 1 and 2 and the blue ones represent the face-sharing between 1 and 3. In Fig. 7(d), the edge connected by two brown atoms displays the edge-sharing between 1 and 4 and the orange atom connects two DISICO

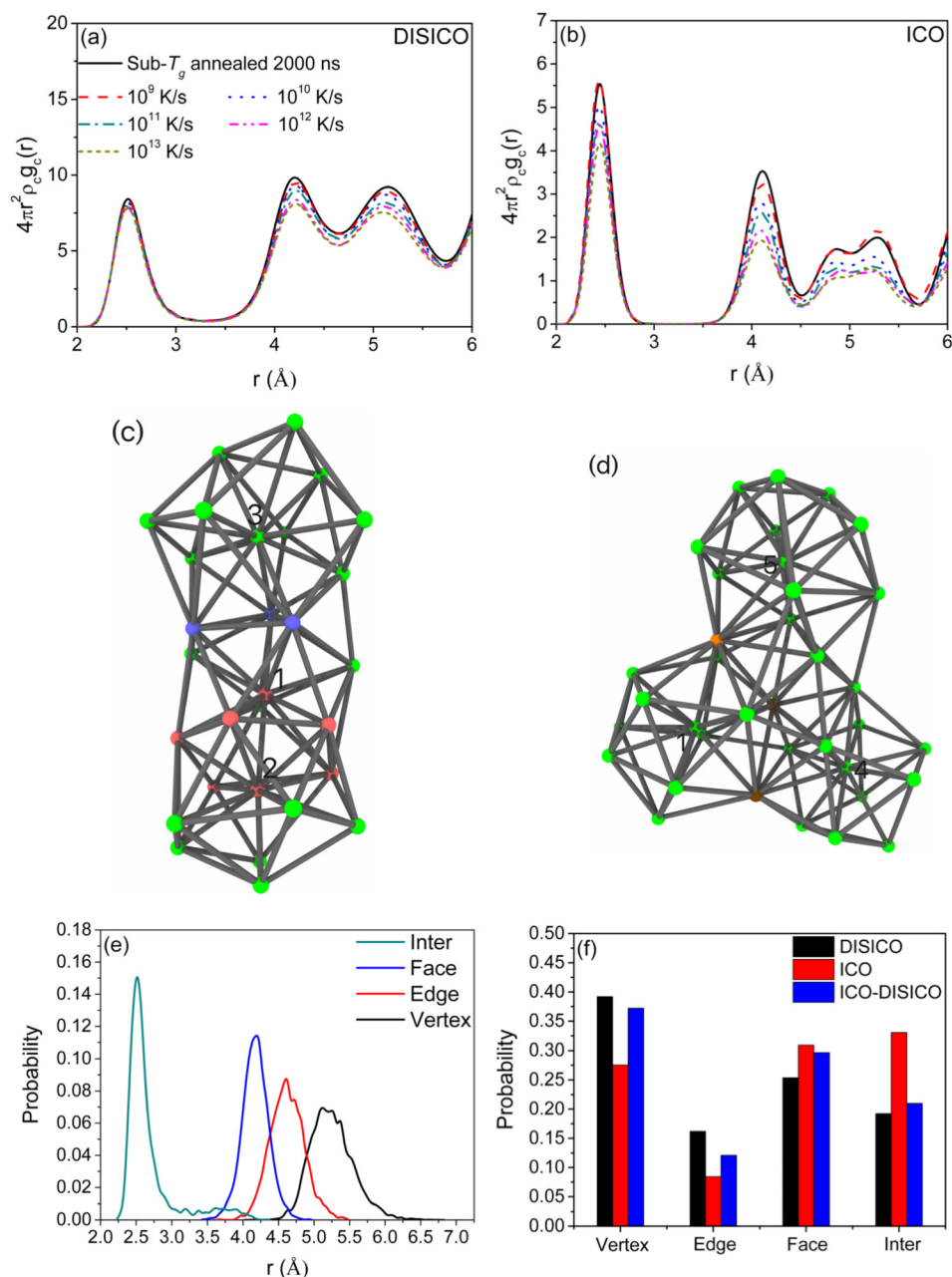


FIG. 7. The radial distribution function calculated by using only the centers of (a) DISICO and (b) ICO in the glassy samples with different cooling processes. (c) and (d) show some typical networks formed by DISICO clusters. The relationship between different DISICO is interpenetrating between DISICO 1 and 2 (in red), face-sharing between 1 and 3 (in blue), edge-sharing between 1 and 4 (in brown), and vertex-sharing between 1 and 5 (in orange). (e) The distributions of the distance between two DISICO centers adopting each type of connection. (f) The distribution of different types of connections for DISICO (in black), ICO (in red), and between ICO + DISICO (in blue). “Vertex,” “Edge,” “Face,” and “Inter” represent vertex-sharing, edge-sharing, face-sharing, and interpenetrating, respectively, in (e) and (f).

indicating vertex-sharing between 1 and 5. The distribution of the distance between two DISICO centers adopting each type of connection is shown in Fig. 7(e). Here, “Vertex” stands for vertex-sharing, “Edge” for edge-sharing, “Face” for face-sharing, and “Inter” for interpenetrating. It can be seen that the first peak in Fig. 7(a) is attributed to interpenetrating, the second peak at around 4.2 Å results from both the face-sharing and edge-sharing, and the third peak at around 5.2 Å is caused by the edge-sharing and vertex-sharing. The distributions of different types of connections for DISICO, ICO, and between ICO and DISICO are shown in Fig. 7(f). It can be clearly seen that DISICO is less likely to be interpenetrated and more likely to be involved in vertex-sharing and edge-sharing compared to ICO, indicating that DISICO is less efficient in geometry packing. For the connection between DISICO and ICO, vertex-sharing and face-sharing are also more popular than interpenetrating.

With the Ni-centered DISICO accounting for almost 50% of the total Ni-centered clusters, it is interesting to see whether the DISICO clusters are percolating^{42,43} or not. Figure 8 shows the centers of the Ni-centered DISICO of the sub- T_g annealed sample at 300 K. If two centers are within the distance of 3 Å, there is a bond connecting them indicating that the two DISICO are interpenetrated. It can be observed that there is a backbone formed by the yellow balls which is percolating in the configuration. In this way, we can show that the centers of the Ni-centered DISICO percolate through the sample and form a backbone in the glass configuration. However, further studies are still needed to give a detailed description of this backbone and relate it with macroscopic properties.

To see the dependence of the MRO on the function of the cooling rate, we examine the fraction of interpenetrating ICO clusters in the ICO networks and the coordination

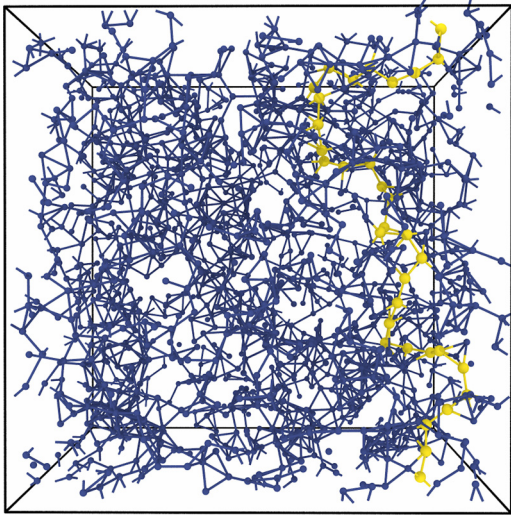


FIG. 8. The centers of the DISICO clusters in the sub- T_g annealed sample at 300 K. If two centers are within the distance of 3 Å, there is a bond connecting them indicating that the two DISICO are interpenetrated. The backbone formed by the yellow balls is percolating in the structure.

numbers of ICO-ICO centers (using a cutoff distance of 3 Å) at different effective cooling rates, respectively. As shown in Fig. 9, with the decreasing cooling rate, more ICO centers are within the cutoff distance of another ICO center and the interpenetrating network becomes more widespread with more ICO centers involved in it. In this perspective, the lower cooling rate increases the number of SROs and enhances the packing in the MRO at the same time, indicating that the real glasses would exhibit highly interconnected and stabilized ICO networks.

F. Connection between the structure and dynamics

Finally, we investigate the relationship between the structure, energy, and dynamics in the glass system during the cooling and annealing process. The dynamics of a system is usually quantified by the mean-square displacements (MSD) of the atoms as a function of time

$$\langle R^2(t) \rangle = \frac{1}{N} \left\langle \sum_{i=1}^N |\mathbf{R}_i(t + \tau) - \mathbf{R}_i(\tau)|^2 \right\rangle, \quad (2)$$

where N is the number of atoms, \mathbf{R}_i are the coordinates of atom i , and τ is the arbitrary origin of time. The self-diffusivity is then calculated using the Einstein's relation

$$D = 1/6 \lim_{t \rightarrow \infty} \partial \langle R^2(t) \rangle / \partial t. \quad (3)$$

In the cooling process, the boom of clusters below 1300 K shown in Fig. 6(b) may be a signature for the “crossover” phenomenon^{36–38} and the diffusion coefficients at different temperatures are presented in Fig. 10(a). It is clear that the deviation from linear Arrhenius relations starts to emerge also at about 1300 K. The crossover from Arrhenius to non-Arrhenius in the dynamics view is connected firmly with the SRO development from the structural point of view. This phenomenon has also been found in several supercooled Lennard-Jones binary mixtures where locally preferred structures are associated with the super-Arrhenius behavior and fragility.⁴⁴ However, the embedded-atom method (EAM) potential used in the present work could describe the interaction between the metal atoms in the system more accurately. In this way, the connection between structures and the “crossover” phenomenon found here not only validates the previous results from the universal Lennard-Jones systems,⁴⁴ but also could give a convincing demonstration on a realistic metallic alloy system. In order to establish the structure-dynamics relationship during the annealing process, first we need to determine a proper time window (Δt). If Δt is too small, the hopping process⁴⁵ would not take place. But if it is too large, the initial structure cannot be preserved. Here, we use the method similar to that in Ref. 46. When we choose $\Delta t = 10$ ns, the mean displacements (square root of MSD) are 1.89 Å and 1.18 Å for Ni and Nb, respectively, as shown in Fig. 10(b). Considering the first peak of $g_{\text{Ni-Ni}}(r)$ and $g_{\text{Nb-Ni}}(r)$ at around 2.49 Å and 2.61 Å, respectively, we believe that the time window of 10 ns can basically preserve the initial structure. We then calculate the self-part of the time-dependent van Hove correlation function⁴⁷ with $\Delta t = 10$ ns and the function is defined as

$$G_S(r, t) = \frac{1}{N} \left\langle \sum_{j=1}^N \delta(r + r_j(0) - r_j(t)) \right\rangle. \quad (4)$$

Figure 10(c) displays the van Hove correlation function at 950 K with $\Delta t = 10$ ns and the multiple small peaks are observed at a long distance which indicates the hopping process. The displacement of cutoff = 1.33 Å is chosen to divide atoms into two groups: (1) immobile atoms whose displacements are less than the cutoff for the time window; (2) mobile atoms in the right side of the cutoff which moves

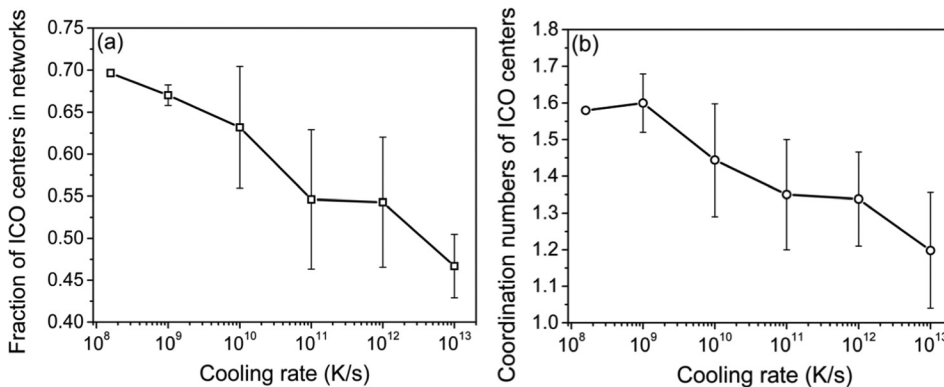


FIG. 9. (a) The fraction of ICO centers in networks at different effective cooling rates and the networks formed by ICO centers are deprived of dimers with a cutoff of 3 Å. (b) The change in coordination numbers between only ICO centers with cooling rates.

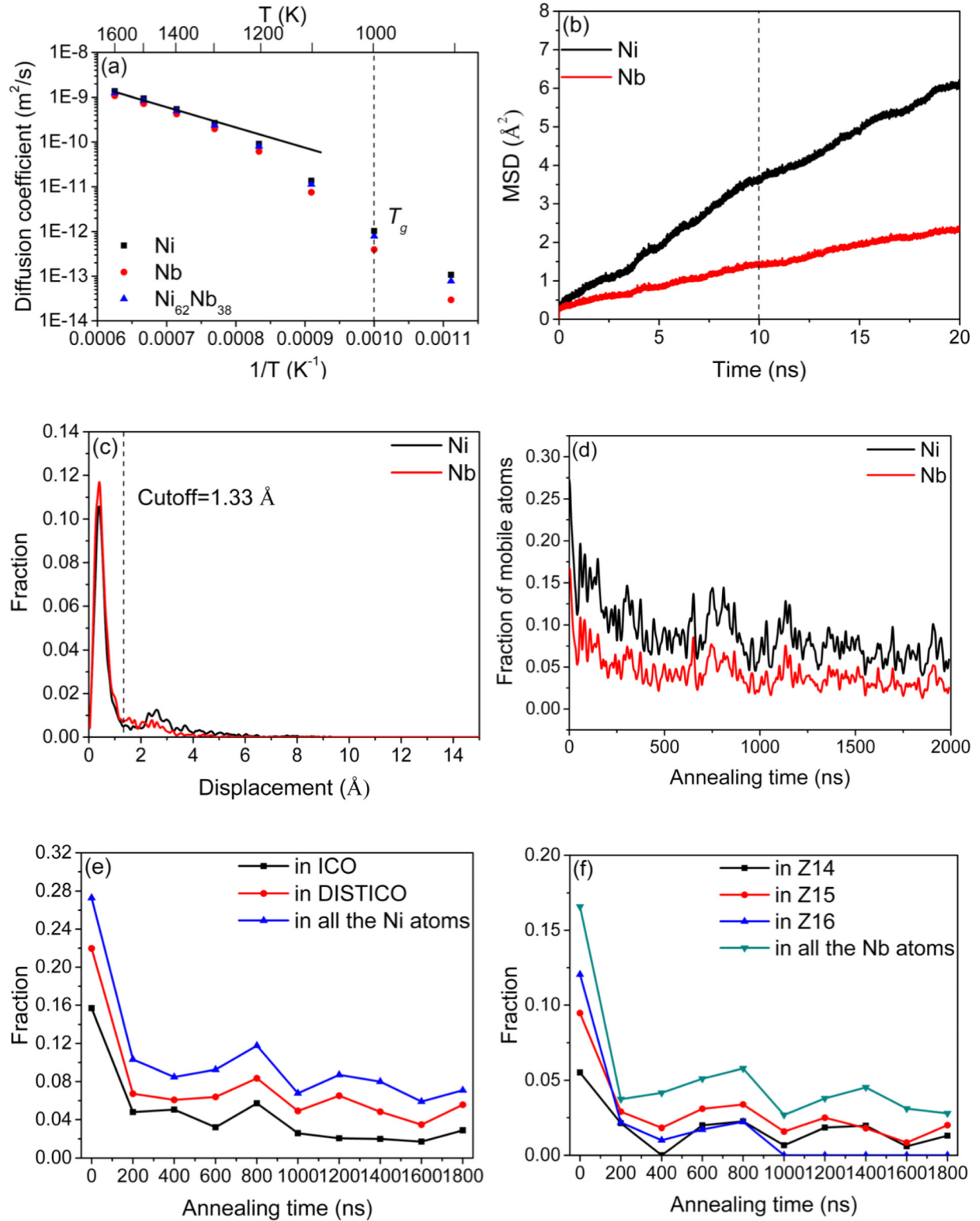


FIG. 10. (a) Diffusion coefficients at different temperatures. (b) The mean-square displacement (MSD) in the first 20 ns of the sub- T_g annealing process. At the time of 10 ns, the mean displacements (square root of MSD) are 1.89 \AA and 1.18 \AA for Ni and Nb, respectively. (c) Van Hove correlation at the beginning of the sub- T_g annealing and the multiple small peaks indicate the existence of hopping processes. The cutoff is chosen at 1.33 \AA to distinguish the mobile and immobile atoms. (d) The fraction of mobile atoms in Ni and Nb at different annealing times. (e) The fraction of mobile atoms belonging to (Ni-centered) ICO and DISTICO centers through the annealing process. (f) The fraction of mobile atoms in (Nb-centered) Z14, Z15, and Z16 centers at different annealing times.

relatively faster as if they are still in the liquid state. In Fig. 10(d), the fraction of mobile atoms in Ni and Nb is plotted. As the annealing process goes on, the fraction of mobile atoms decreases for both Ni and Nb. The fraction of mobile

atoms is lower in Nb because Nb atoms diffuse more slowly than Ni as can be seen in Fig. 10(b). Then, we investigate the relationship between different motifs and dynamics. Figures 10(e) and 10(f) display the fraction of mobile atoms

belonging to the center of each motif for Ni- and Nb-centered clusters, respectively. For Ni-centered motifs, the fraction of mobile atoms is the lowest in ICO center. DISICO, with some distortions from ICO, exhibit a larger fraction of mobile atoms but still lower than that of all Ni atoms. As for the Nb-centered SROs, the centers of Z14, Z15, and Z16 are slower compared to the average level. Icosahedrally structured domains with slow dynamics which grow with cooling have also been found in a simple mon-atomic glass-forming liquid by MD with Lennard-Jones potential.⁴⁸ Besides, the formation of stable domains like icosahedral structures is found to correspond to deeper traps in the potential energy surface in Lennard-Jones mixtures.⁴⁹ In another binary metallic glass system, Cu-Zr, Zhang *et al.*⁵⁰ provided a statistical way to identify mobile and immobile atoms and found that immobile atoms exhibit a predominantly ICO order and mobile atoms are with the low symmetry packing. Douglas *et al.*⁵¹ built a relationship between the picosecond (“fast”) dynamics and long-time structural relaxation over the full range of temperatures and alloys compositions of Cu-Zr and the self-diffusion coefficients could be predicted by the relationship in conjunction with the Fractional Stokes-Einstein (FSE) relation.⁵² However, the structure-dynamics correlation is also found to be system dependent in recent years.^{53–55} Widmer-Cooper and Harrowell⁵³ reported that the short-time fluctuations could predict the spatial distribution of the long-time dynamic propensities pretty well in a simulated 2D glass-forming mixture. Hocky *et al.*⁵⁴ found that the correlation between the structure and dynamics is only strong in systems that deviate from the mean-field picture of glassy dynamics by studying four different Lennard-Jones mixtures. Jack *et al.*⁵⁵ demonstrated that the correlation between dynamics and low energy local structures is rather weak in two Lennard-Jones systems. For the system in the present paper, SROs exhibiting more sluggish mobility develop in the sub- T_g annealing process, which are connected to the lower potential energy and the dynamical slowdown for the system. A similar connection has also been found in polydisperse colloidal liquids by Kawasaki and Tanaka,⁵⁶ where the origin of cooperative slow dynamics is the growth of a critical-like static order associated with low free energy. However, the bond orientational order method⁵⁷ used in Ref. 56 may not be valid for binary systems with different sized particles.^{58–61} In this light, the connection found in the present paper validates and extends the conclusion in Ref. 56.

IV. CONCLUSIONS

In this work, we carried out molecular dynamics study on a Ni₆₂Nb₃₈ bulk MG forming system with the newly developed EAM potential. First, the glass transition temperature is determined to be around 1000 K and the sub- T_g annealing process is employed at 950 K for 2.0 μ s. A well-relaxed glassy sample with lower potential energy is then achieved when cooled to 300 K. The structure factor of the sub- T_g annealed sample agrees better with experiment than that of the continuously quenched samples at a higher cooling rate. Then, the state-of-the-art structural analysis

algorithms such as cluster alignment and pair-wise alignment methods are applied to investigate and characterize the SROs. A distorted ICO (DISICO) motif is excavated and has a fraction of almost 50% of Ni-centered clusters in the sub- T_g annealed sample. The dominant DISICO and ICO imply good GFA of this system. A chemical order characterization method at each position of the motif is achieved based on the alignment method. The DISICO and ICO exhibit about the same total fraction of Nb atoms in the motifs. When it comes to each position, DISICO show rather uneven distribution of the fraction of Nb atoms compared to ICO. In the cooling process, the SRO starts to develop at around 1300 K which corresponds to the temperature where the deviation from Arrhenius relation emerges for the diffusion coefficient. In this way, the “crossover” phenomenon is connected firmly with the structural order. With a lower effective cooling rate, the fraction of the SRO increases and the MRO is enhanced. For DISICO, they exhibit lower possibility to be interpenetrated than ICO, which deteriorates their packing efficiency. With almost 50% of Ni-centered clusters as DISICO, the DISICO centers form a backbone which is percolating through the sample. As for ICO, the fraction of ICO centers in the interpenetrating networks and the coordination numbers of ICO-ICO centers increase with decreasing cooling rate indicating a denser packed ICO network. In the annealing process, the increase of the SRO with sluggish mobility explains the lower potential energy and the dynamical slowdown of the system.

ACKNOWLEDGMENTS

Work at Ames Laboratory was supported by the U.S. Department of Energy (DOE), Office of Science, Basic Energy Sciences, Materials Science and Engineering Division including a grant of computer time at the National Energy Research Supercomputing Center (NERSC) in Berkeley. Ames Laboratory is operated for the U.S. DOE by Iowa State University under Contract # DE-AC02-07CH11358. T. Q. Wen and N. Wang would like to acknowledge the financial support from the National Natural Science Foundation of China (Grant Nos. 51671160 and 51271149). L. Tang acknowledges the support from the National Natural Science Foundation of China (Grant Nos. 11304279 and 11364007). Z. J. Yang acknowledges the Natural Science Foundation of Zhejiang Province, China (Grant No. LY18E010007).

¹W. Klement, R. H. Willens, and P. Duwez, *Nature* **187**, 869 (1960).

²D. B. Miracle, *Nat. Mater.* **3**, 697 (2004).

³H. W. Sheng, W. K. Luo, F. M. Alamgir, J. M. Bai, and E. Ma, *Nature* **439**, 419 (2006).

⁴Y. Q. Cheng, E. Ma, and H. W. Sheng, *Phys. Rev. Lett.* **102**, 245501 (2009).

⁵D. Ma, A. D. Stoica, and X. L. Wang, *Nat. Mater.* **8**, 30 (2009).

⁶M. W. Chen, *Annu. Rev. Mater. Res.* **38**, 445 (2008).

⁷W. H. Wang, *Prog. Mater. Sci.* **57**, 487 (2012).

⁸T. Egami, T. Iwashita, and W. Dmowski, *Metals* **3**(1), 77 (2013).

⁹J. Das, M. B. Tang, K. B. Kim, R. Theissmann, F. Baier, W. H. Wang, and J. Eckert, *Phys. Rev. Lett.* **94**, 205501 (2005).

¹⁰Y. Q. Cheng and E. Ma, *Prog. Mater. Sci.* **56**, 379 (2011).

¹¹J. Ding and E. Ma, *npj Comput. Mater.* **3**, 9 (2017).

¹²A. Inoue, *Acta Mater.* **48**, 279 (2000).

- ¹³D. H. Xu, B. Lohwongwatana, G. Duan, W. L. Johnson, and C. Garland, *Acta Mater.* **52**, 2621 (2004).
- ¹⁴A. Inoue and W. Zhang, *Mater. Trans.* **45**, 584 (2004).
- ¹⁵M. B. Tang, D. Q. Zhao, M. X. Pan, and W. H. Wang, *Chin. Phys. Lett.* **21**, 901 (2004).
- ¹⁶D. Wang, Y. Li, B. B. Sun, M. L. Sui, K. Lu, and E. Ma, *Appl. Phys. Lett.* **84**, 4029 (2004).
- ¹⁷J. Pu, J. F. Wang, J. Z. Xiao, and K. Cui, *Trans. Nonferrous Met. Soc. China* **13**, 1056 (2003).
- ¹⁸H. S. Chen and K. A. Jackson, *Metallic Glasses* (ASM International, Metals Park, Ohio, 1978).
- ¹⁹Z. W. Zhu, H. F. Zhang, D. G. Pan, W. S. Sun, and Z. Q. Hu, *Adv. Eng. Mater.* **8**, 953 (2006).
- ²⁰L. Xia, W. H. Li, S. S. Fang, B. C. Wei, and Y. D. Dong, *J. Appl. Phys.* **99**, 026103 (2006).
- ²¹A. Inoue, *Prog. Mater. Sci.* **43**, 365 (1998).
- ²²F. Zhang, M. Ji, X. W. Fang, Y. Sun, C. Z. Wang, M. I. Mendelev, M. J. Kramer, R. E. Napolitano, and K. M. Ho, *Acta Mater.* **81**, 337 (2014).
- ²³L. Ward, D. Miracle, W. Windl, O. N. Senkov, and K. Flores, *Phys. Rev. B* **88**, 134205 (2013).
- ²⁴Y. Sun, F. Zhang, Z. Ye, Y. Zhang, X. W. Fang, Z. J. Ding, C. Z. Wang, M. I. Mendelev, R. T. Ott, M. J. Kramer, and K. M. Ho, *Sci. Rep.* **6**, 23734 (2016).
- ²⁵T. Ohkudo and Y. Hirotsu, *Mater. Sci. Eng., A* **217–218**, 388 (1996).
- ²⁶J. Ding, Y. Q. Cheng, and E. Ma, *Acta Mater.* **69**, 343 (2014).
- ²⁷H. Tian, H. Liu, C. Zhang, J. J. Zhao, C. Dong, and B. Wen, *J. Mater. Sci.* **47**, 7628 (2012).
- ²⁸Y. Zhang, R. Ashcraft, M. I. Mendelev, C. Z. Wang, and K. F. Kelton, *J. Chem. Phys.* **145**, 204505 (2016).
- ²⁹M. W. Finnis and J. E. Sinclair, *Philos. Mag. A* **50**, 45 (1984).
- ³⁰T. D. Xu, X. D. Wang, H. Zhang, Q. P. Cao, D. X. Zhang, and J. Z. Jiang, *J. Chem. Phys.* **147**, 144503 (2017).
- ³¹F. Zhang, M. I. Mendelev, Y. Zhang, C. Z. Wang, M. J. Kramer, and K. M. Ho, *Appl. Phys. Lett.* **104**, 061905 (2014).
- ³²Y. Zhang, F. Zhang, C. Z. Wang, M. I. Mendelev, M. J. Kramer, and K. M. Ho, *Phys. Rev. B* **91**, 064105 (2015).
- ³³Y. Sun, Y. Zhang, F. Zhang, Z. Ye, Z. J. Ding, C. Z. Wang, and K. M. Ho, *J. Appl. Phys.* **120**, 015901 (2016).
- ³⁴X. W. Fang, C. Z. Wang, Y. X. Yao, Z. J. Ding, and K. M. Ho, *Phys. Rev. B* **82**, 184204 (2010).
- ³⁵X. W. Fang, L. Huang, C. Z. Wang, K. M. Ho, and Z. J. Ding, *J. Appl. Phys.* **115**, 053522 (2014).
- ³⁶T. Q. Wen, W. J. Yao, and N. Wang, *Sci. Rep.* **7**, 13164 (2017).
- ³⁷T. Iwashita, D. M. Nicholson, and T. Egami, *Phys. Rev. Lett.* **110**, 205504 (2013).
- ³⁸A. Jaiswal, T. Egami, K. F. Kelton, K. S. Schweizer, and Y. Zhang, *Phys. Rev. Lett.* **117**, 205701 (2016).
- ³⁹S. Plimpton, *J. Comput. Phys.* **117**, 1 (1995).
- ⁴⁰T. Q. Wen, L. Tang, Y. Sun, K. M. Ho, C. Z. Wang, and N. Wang, *Phys. Chem. Chem. Phys.* **19**, 30429 (2017).
- ⁴¹P. H. Gaskell, *Amorphous Metals* (World Scientific Publishing, Singapore, 1985).
- ⁴²V. K. S. Shante and S. Kirkpatrick, *Adv. Phys.* **20**, 325–357 (1971).
- ⁴³D. Z. Chen, C. Y. Shi, Q. An, Q. S. Zeng, W. L. Mao, W. A. Goddard, and J. R. Greer, *Science* **349**, 1306 (2015).
- ⁴⁴D. Coslovich and G. Pastore, *J. Chem. Phys.* **127**, 124504 (2007).
- ⁴⁵M. C. C. Ribeiro, *Phys. Chem. Chem. Phys.* **6**, 771 (2004).
- ⁴⁶Y. Zhang, C. Z. Wang, F. Zhang, M. I. Mendelev, M. J. Kramer, and K. M. Ho, *Appl. Phys. Lett.* **105**, 151910 (2014).
- ⁴⁷L. V. Hove, *Phys. Rev.* **95**, 249 (1954).
- ⁴⁸M. Dzugutov, S. I. Simdyankin, and F. H. M. Zetterling, *Phys. Rev. Lett.* **89**, 195701 (2002).
- ⁴⁹D. Coslovich and G. Pastore, *J. Chem. Phys.* **127**, 124505 (2007).
- ⁵⁰H. Zhang, C. Zhong, J. F. Douglas, X. D. Wang, Q. P. Cao, D. X. Zhang, and J. Z. Jiang, *J. Chem. Phys.* **142**, 164506 (2015).
- ⁵¹J. F. Douglas, B. A. P. Betancourt, X. H. Tong, and H. Zhang, *J. Stat. Mech.* **2016**, 054048.
- ⁵²J. F. Douglas and D. Leporini, *J. Non-Cryst. Solids* **235–237**, 137 (1998).
- ⁵³A. Widmer-Cooper and P. Harrowell, *Phys. Rev. Lett.* **96**, 185701 (2006).
- ⁵⁴G. M. Hocky, D. Coslovich, A. Ikeda, and D. R. Reichman, *Phys. Rev. Lett.* **113**, 157801 (2014).
- ⁵⁵R. L. Jack, A. J. Dunleavy, and C. P. Royall, *Phys. Rev. Lett.* **113**, 095703 (2014).
- ⁵⁶T. Kawasaki and H. Tanaka, *Phys. Rev. E* **89**, 062315 (2014).
- ⁵⁷P. J. Steinhardt, D. R. Nelson, and M. Ronchetti, *Phys. Rev. B* **28**, 784 (1983).
- ⁵⁸H. Tanaka, *Eur. Phys. J. E* **35**, 113 (2012).
- ⁵⁹B. Charbonneau, P. Charbonneau, and G. Tarjus, *Phys. Rev. Lett.* **108**, 035701 (2012).
- ⁶⁰H. Tanaka, *Faraday Discuss.* **167**, 9 (2013).
- ⁶¹D. N. Perera and P. Harrowell, *J. Chem. Phys.* **111**, 5441 (1999).